Dalton Transactions

Accepted Manuscript

ROYAL SOCIETY OF CHEMISTRY

www.rsc.org/dalton

Journal Name

RSCPublishing

COM

Cite this: DOI: 10.1039/x0xx00000x

Microporous $Ni_{11}(HPO_3)_8(OH)_6$ nanocrystals for high performance flexible asymmetric all solid-state supercapacitors

Received 00th January 2012,
Accepted 00th January 2012

DOI: 10.1039/x0xx00000x

www.rsc.org/

Yanping Gao,[a] Junhong Zhao,[a] Zhen Run,[a] Guangqin Zhang[a] and Huan Pang[a,b]*

Microporous $Ni_{11}(HPO_3)_8(OH)_6$ nanocrystals are prepared by a hydrothermal method, which are successfully applied as a positive electrode of a flexible all solid-state asymmetric supercapacitor. Due to the specific micro/nanostructure, the flexible solid-state asymmetric supercapacitor can achieve a maximum energy density of 0.45 mWh·cm^{-3}, which is higher than most of reported supercapacitors. More importantly, the device also offers efficiency cycle ability for 10000 cycles.

Introduction

Metal phosphates recently receive a lot of research for their broad applications in many fields.[1-14] Li et al have successfully reported a preparation process to synthesize an array of transition-metal phosphate amorphous colloidal spheres.[1] Crystalline microporous transition-metal phosphites $M_{11}(HPO_3)_8(OH)_6$ (M = Zn, Co, and Ni) have been firstly reported by Marcos et al in 1993.[6, 7] The shape and size of inorganic nanomaterials are regarded as critical factors in varying their electrical, optical, electrochemical and other properties.[15] Some efforts have been focused on the preparation of metal phosphate-based micro/nanostructures.[16-21] In spite of some great developments, to the best of our knowledge, there are few reports about preparation of $Ni_{11}(HPO_3)_8(OH)_6$ micro/nanocrystals so far.

Recently, asymmetric supercapacitors (ASCs) which have a battery type Faradaic electrode as a high energy density and power density electrode as a power source are a promising alternative to traditional structured supercapacitors (SCs).[22-27] According to the electrolyte, ASCs can be divided into two categories: 1) Aqueous ASCs. For example, graphene-MnO_2//activated carbon nanofiber,[22] $Ni(OH)_2$-graphene and graphene,[27] and $Ni(OH)_2$-nanowires//CMK-5.[28] However, aqueous ASC device fabrication usually requires high-cost encapsulation techniques to avoid the possible leakage of electrolytes, which makes the fabrication of small and flexible devices difficult. 2) Solid state ASCs. Recently, Lu et al have successfully reported a solid-state ASC based on $Ni(OH)_2$-nanowire //Ordered mesoporous carbon,[29] H-TiO_2@MnO_2//H-TiO_2@C core–shell nanowires.[30] Solid-state ASCs have advantages such as small-size, light-weight, ease of handing, excellent reliability, and a wider range of operating temperatures, suitable for the next-generation portable and flexible devices, however, there are few reports about the fabrication of solid-state ASCs. It is surely a challenge to make low-cost, high-performance solid state ASCs.

In this work, we report on a study of the hydrothermal synthesis of microporous $Ni_{11}(HPO_3)_8(OH)_6$ nanocrystals and their application for high-performance flexible solid-state asymmetric supercapacitors. More importantly, the electrochemical results show that the assembled microporous $Ni_{11}(HPO_3)_8(OH)_6$ nanocrystals//Graphene nanosheets ASCs achieve a maximum energy density of 0.45 mWh·cm^{-3}, which is higher than most of reported solid state SCs, and high cycle stability for 10000 cycles, which makes the material as one of the most promising candidates for high-performance flexible solid-state asymmetric supercapacitors in the field of energy storage devices.

Results and discussion

Figure 1a shows XRD patterns of as-prepared samples. All peaks of the pattern are indexed to be in agreement with $Ni_{11}(HPO_3)_8(OH)_6$ (JCPDS No.81-1065). No peaks of other phosphites or phosphates were detected from these patterns. In the inset of Figure 1a, the schematic crystal structures of $Ni_{11}(HPO_3)_8(OH)_6$ super cells (2×2×2 slabs) are projected based on the data of ICSD-72432. $Ni_{11}(HPO_3)_8(OH)_6$ super cells (A higher magnefication image is shown in **Figure S1** of Electronic Supplementary Information (**ESI**) are in the hexagonal arrangement, with the octahedra formimg two kinds of channels. The smaller triangular ones, surrounded by three $(Ni_4O_{12})_n$ chains, are occupied by 2/8 of the HPO_3^{2-} pseudotetrahedral groups. The remaining (6/8) phosphite groups are located on the walls of the larger hexagonal channels. These channels may offer many accesses and pathways to improve the diffusion of ions and electrolyte. From the low-angle XRD pattern in **Figure S2** of ESI, there is a peak at 1.33°. From such strong signal, it is clear that there are uniform micropores in the as-prepared $Ni_{11}(HPO_3)_8(OH)_6$.

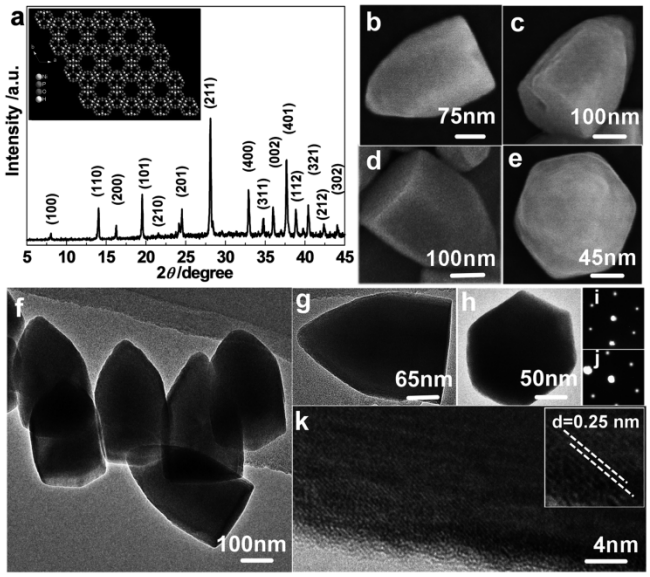

Figure 1. a) XRD patterns of as-prepared samples and corresponding JCPDS No. 81-1065, $Ni_{11}(HPO_3)_8(OH)_6$, Inset-The schematic crystal structures of $Ni_{11}(HPO_3)_8(OH)_6$ super cell (2×2×2 slabs) projected based on data of Inorganic Crystal Structure Data (ICSD)-72432, b-e) SEM images, f-h, k) TEM images, and i, j) Corresponding SAED patterns.

The morphology of as-prepared $Ni_{11}(HPO_3)_8(OH)_6$ is examined by field emission scanning electron microscopy (FE-SEM), and transmission electron microscopy (TEM). A typical low-magnification SEM image in Figure 1b-e shows that the morphology of the as-prepared samples is the hexagonal pyramidal with the length of 300 nm from different view-directions. In addition, the diameter of the big end of the single hexagonal pyramidal is about 195 nm in Figure 1e, which futher comfirms the hexagonal structure. Figure 1f shows the TEM image of several uniform $Ni_{11}(HPO_3)_8(OH)_6$ nanocrystals. TEM images of the single $Ni_{11}(HPO_3)_8(OH)_6$ nanocrystal and the big end are shown in Figure 1g, h. Their corresponding SAED patterns are shown in Figure 1i, j. They show that the $Ni_{11}(HPO_3)_8(OH)_6$ nanocrystal is structurally uniform in the atom-scale, and may be described as a single crystal. What's more, from HRTEM images in the Figure 1k and its inset-image, the measured distance of neighboring lattice fringes is ~0.25 nm, corresponding well to the (002) lattice spacing (0.245 nm) of $Ni_{11}(HPO_3)_8(OH)_6$ (JCPDS No.81-1065). The channels of the specific micropous $Ni_{11}(HPO_3)_8(OH)_6$ crystal is also seen in the **Figure S3**. The diameter of the channels is 0.74 nm in Figure S3d, which further indicates the as-prepared $Ni_{11}(HPO_3)_8(OH)_6$ nanocrystals provide many channels for electrolytes and ions.

Gas sorption properties of the as-prepared $Ni_{11}(HPO_3)_8(OH)_6$ crystal are also studied. N_2 adsorption and desorption isotherms of the samples with different morphologies are shown in **Figure S4**. All the samples show a characteristic Type I sorption isotherm, which is typical for microporous materials with high amounts of nitrogen adsorption. The as-prepared $Ni_{11}(HPO_3)_8(OH)_6$ crystal has a large BET surface of 398 $m^2 g^{-1}$, which indicates an excellent BET surface of microporous $Ni_{11}(HPO_3)_8(OH)_6$ crystals. The hysteresis loops in the isotherms are further shown in the Barrett-Joyner-Halenda (BJH) pore size distribution curves (Figure S4b). The average pore diameter of as-prepared samples is around 0.7 nm by using the method of Horvath-Kawazoe (HK). It is well known that the micropore plays a critical role in electrochemical processes, due to their capability of facilitating mass diffusion/transport (e.g., electrolyte penetration, and guest molecule/ion transport) and ensuring a high electroactive surface area. Therefore, the microporous texture of the $Ni_{11}(HPO_3)_8(OH)_6$ crystals is likely to affect its performance in electrochemical applications.

Figure 2a shows the cyclic voltammogram (CV) curves of as-prepared $Ni_{11}(HPO_3)_8(OH)_6$ nanocrystal electrode in the potential range of 0 to 0.6 V (vs. Hg/HgO) in 3.0 M KOH electrolyte solution at different scan rates of 5-30 $mV \cdot s^{-1}$ in a conventional three-electrode system. As is shown, the current response increased with the scan rate, and the shapes are different from that of electric double-layer capacitance, suggesting that the capacity mainly results from pseudocapacitive capacitance. We also try to propose the reversible redox reactions in $Ni_{11}(HPO_3)_8(OH)_6$ nanocrystal electrode, where HS stands for hydrophosphite group [-$(HPO_3)_8(OH)_6$]:

$$HS\text{-}Ni(II) + OH^-_{sol} \Leftrightarrow HS\text{-}(OH^-)Ni(III) + e^- \quad (1)$$

Figure 2b shows chronopotentiometry (CP) curves at different current densities. The symmetrical characteristic of charging/discharging curves is good, which means that the $Ni_{11}(HPO_3)_8(OH)_6$ nanocrystal electrode with excellent electrochemical capability and redox process are reversible. The relationships between the specific capacitances calculated by CP curves and current densities are given in Figure 2c. Based on the CP curves, the $Ni_{11}(HPO_3)_8(OH)_6$ nanocrystal electrode has the large specific capacitance and reaches up to 558 $F \cdot g^{-1}$ at a current density of 0.5 $A \cdot g^{-1}$, and remains at 224 $F \cdot g^{-1}$ even at 7.0 $A \cdot g^{-1}$. The cycling life test is also measured as shown in Figure 2d, it is seen that the specific capacitance is retained at 545 $F \cdot g^{-1}$ even after 10000 cycles.

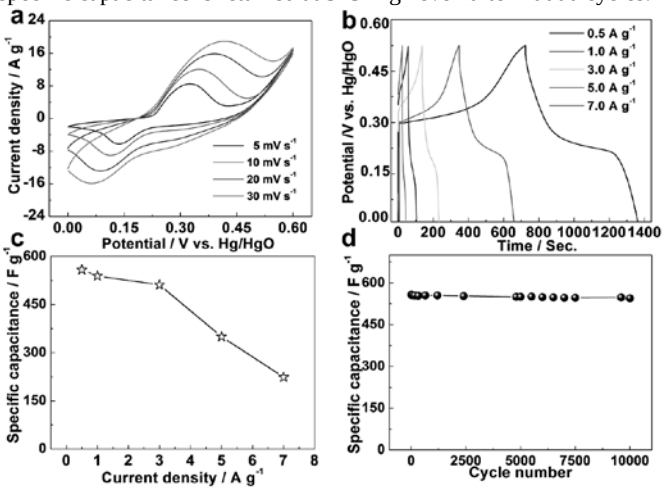

Figure 2. a) Cyclic voltammetry within a 0 to 0.6 V range at a scan rate 5-30 $mV \cdot s^{-1}$ were performed on the $Ni_{11}(HPO_3)_8(OH)_6$ nanocrystal electrode in 3.0 M KOH at room temperature, b) The galvanostatic charge–discharge curves during current densities, 0.5-7.0 $A \cdot g^{-1}$, c) Specific capacitance obtained from different current densities, and d) Cycling life test at 0.5 $A \cdot g^{-1}$ for 10000 cycles.

With the dream to develop flexible power sources, a flexible solid-state asymmetric supercapacitor ($Ni_{11}(HPO_3)_8(OH)_6$//Graphene) was further fabricated using the microporous $Ni_{11}(HPO_3)_8(OH)_6$ nanocrystal and the graphene nanosheet as active materials (Detailed information seen in Experimental Section) by our previous method.[31] **Figure 3**a shows a series of CV measurements of the $Ni_{11}(HPO_3)_8(OH)_6$//Graphene ASC with different cell voltages varying from 0.0-0.72 V to 0.0-1.40 V. When the operating potential is 0.72 V, the presence of ambiguous redox peaks (In the region between 0.0 and 0.72 V) indicates that the pseudocapacitive properties of the cell originate from the positive electrode (The microporous $Ni_{11}(HPO_3)_8(OH)_6$ nanocrystal). With the operating potential increasing to 1.40 V, more Faradic reactions occurred. In

order to test the flexibility of our solid-state ASC, the solid-state ASC was bended with different angles (Figure 3b), while corresponding electrochemical tests were conducted. CV measurements were conducted at a scan rate of 30 mV s^{-1} with different bending angles, as shown in Figure 3b, the CV curves with different bending angles changes lightly. Remarkably, throughout the bending processes, the specific capacitance of the device is maintained. Galvanostatic charge-discharge curves of the ASCs at various current densities are shown in Figure 3c. The corresponding specific capacitance is shown in Figure 3d, the specific capacitance reaches 1.64 F·cm^{-3} at a current density of 0.50 mA·cm^{-2}, and even reaches 1.10 F·cm^{-3} at 5.0 mA·cm^{-2}

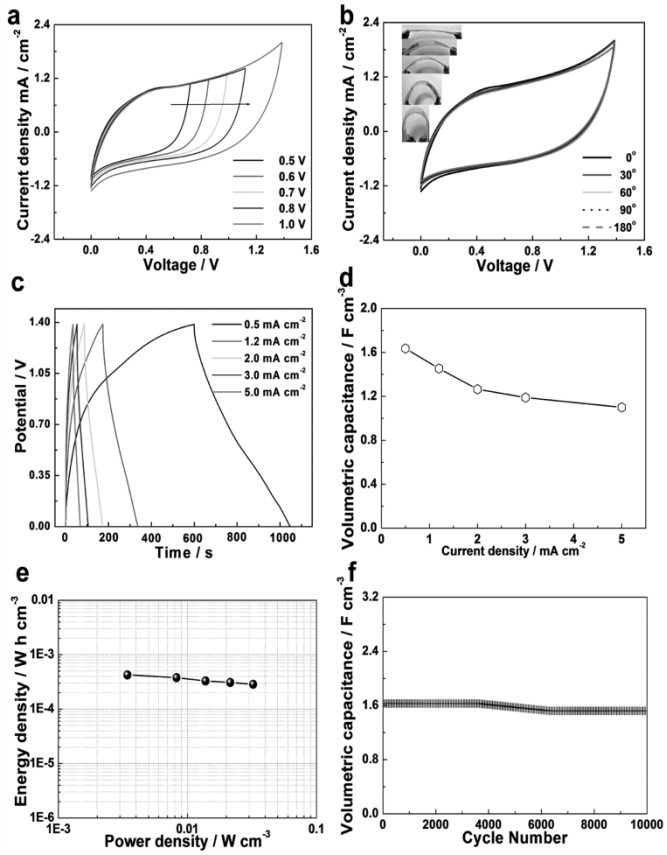

Figure 3. a) CV curves of $Ni_{11}(HPO_3)_8(OH)_6$//Graphene ASCs with the increase of the potential window, b) CV curves within a 0-1.40 V range at a scan rate 30 mV s^{-1} with different bended degrees (0^o-180^o), c) The galvanostatic charge-discharge curves during current densities, 0.5-5.0 mA·cm^{-2}, d) Corresponding specific capacitance obtained from discharge curves during current densities, 0.5-5.0 mA·cm^{-2}, e) Ragone plots of the $Ni_{11}(HPO_3)_8(OH)_6$//Graphene ASCs, and f) Cycle life testing at 0.5 mA·cm^{-2}.

The energy and power densities of the flexible solid-state ASCs measured in the potential window of 0-1.40 V at different scan rates are shown in Figure 3e. Figure 3e also compares the volumetric power and energy densities of all the flexible solid-state ASCs reported in this work to the values reported for other energy storage devices. The $Ni_{11}(HPO_3)_8(OH)_6$//Graphene ASC device is able to possess a maximum volumetric energy density of 0.45 mW·h·cm^{-3} at a current density of 0.5 mA·cm^{-2}, and 0.30 mW·h·cm^{-3} at 5.0 mA·cm^{-2}, again confirming the good rate performance of the $Ni_{11}(HPO_3)_8(OH)_6$//Graphene ASC device. Moreover, the obtained maximum volumetric energy density is considerably higher than those of recently reported symmetric supercapacitor devices (SSCs) [24, 32-34] and comparable to some developed ASCs,[30, 35-37] such as TiO_2@MnO_2//TiO_2@C-ASCs (0.30 mW·h·cm^{-3}, 0.5 mA·cm^{-2}),[30] ZnO@MnO//Graphene-ASCs (0.234 mW·h·cm^{-3}, 0.5 mA·cm^{-2})[36] and MnO_2//Fe_2O_3-ASCs (0.41 mW·h·cm^{-3}, 0.5 mA·cm^{-2}).[37] Additionally, the $Ni_{11}(HPO_3)_8(OH)_6$//Graphene-ASC device can deliver a maximum power density of 33 mW·cm^{-3} at a current density of 5.0 mA·cm^{-2}, which is much higher than that of the recently reported ZnO@MnO_2-SSCs,[34] and ZnO@MnO_2//Graphene-ASCs,[36] but lower than that of devices based on carbon materials or metal nitrides.[30,32,33] The results above confirm that the $Ni_{11}(HPO_3)_8(OH)_6$//Graphene ASC device is very promising as a high energy-density anode material for ASCs.

What's more, it is found that the flexible solid-state ASCs shows good rate capability at 0.5 mA·cm^{-2}: 100% retention after 2000 cycles and 93.3% retention after 10000 cycles in Figure 3f. The stable cycling performance of the $Ni_{11}(HPO_3)_8(OH)_6$//Graphene ASC device is better than the values reported for other aqueous and solid state ASCs, such as RuO_2/graphene//graphene (95% after 2000 cycles),[38] MnO_2 NW/graphene//graphene (79% after 1000 cycles),[39] PANI/CNT//PANI/CNT (88.6% after 1000 cycles).[40] In comparison to the aqueous electrolyte, solid-state electrolytes can suppress the dissolution of active materials, and can improve the cycling stability.

Conclusions

In summary, microporous $Ni_{11}(HPO_3)_8(OH)_6$ nanocrystals are successfully prepared by the hydrothermal reaction. Flexible solid-state ASC devices based on the microporous $Ni_{11}(HPO_3)_8(OH)_6$ nanocrystal//Graphene-ASC devices are assembled, and the $Ni_{11}(HPO_3)_8(OH)_6$//Graphene ASC device shows great performance, representing the first report of this material applied for supercapacitors. The flexible solid-state device shows little capacitance change after over 10000 charge/discharge cycles at a current density of 0.5 mA·cm^{-2}, and shows an excellent cycling stability with only ~6.7 % decay. Notably, the device shows excellent mechanical flexibility with a bending angle of 0^o up to 180^o. Due to the simplicity and eco-friendly nature of materials synthesis and device fabrication processes, this flexible solid-state asymmetric supercapacitor could be integrated into many power-on-chip systems, roll-up display panels and solar energy harvesters.

Experimental Section

Synthesis of the microporous $Ni_{11}(HPO_3)_8(OH)_6$ nanocrystals: In a typical synthesis, 0.131 g $NiSO_4·6H_2O$, 0.05 g PVP-K30 (Polyvinylpyrrolidone), 0.190 g Trisodiumphosphate, and 20 mL H_2O were mixed together. Then the mixture was transferred into 50 mL stainless-steel autoclaves lined with poly(tetrafluoroethylene) (PTFE, Teflon), which was sealed and maintained at 200 ^oC for 40 h. The obtained precipitates were washed several times by deionized water, ethanol, and dried in the air. The prouduct is directly applied as the positive electrode material.

Preparation of graphite oxide:[23] GO was produced from natural graphite powders (universal grade, 99.985%) according to Hummers method. Firstly, natural graphite powders were treated by 5% HCl twice, then filtered, washed with distilled water thoroughly, and dried at 110 ◦C for 24 h. Secondly, graphite powders (10 g) were placed in cold (0 ^oC) concentrated H_2SO_4 (230 mL), $KMnO_4$ (30 g) was added gradually with stirring and cooling, and the temperature of the solution was not allowed to go up to 20 ^oC. The mixture was stirred for 40 min, and distilled water (460 mL) was added slowly to an increase in temperature to 98 ^oC. The temperature was held at 35±3 ^oC for 30 min. Finally, distilled water (1.4 L) and 30% H_2O_2 solution (100 mL) were added after the reaction. The solution was held at room temperature for 24 h and then the mixture was filtered, washed with 5% HCl aqueous solution until sulfate could not be

detected with $BaCl_2$. The reaction product was dried under vacuum at 50 °C for 24 h.

Preparation of functionalized graphene sheets: [23] The dried GO was thermally exfoliated at 300 °C for 5 min under air atmosphere. The obtained samples were subsequently treated at 700 °C in Ar for 3 h with a heating rate of 2 °C/min. The prouduct is directly applied as the negative electrode material.

Characterizations: The morphology of as-prepared samples was observed by a JEOL JSM-6701F field-emission scanning electron microscope (FE-SEM) at an acceleration voltage of 5.0 kV. The phase analyses of the samples were performed by X-ray diffraction (XRD) on a Rigaku-Ultima III with Cu K_α radiation (λ=1.5418 Å). Transmission electron microscopy (TEM) images were captured on the JEM-2100 instrument microscopy at an acceleration voltage of 200 kV. Nitrogen adsorption-desorption measurements were performed on a Gemini VII 2390 Analyzer at 77 K by using the volumetric method. The specific surface area was obtained from the N_2 adsorption–desorption isotherms and was calculated by using the Brunauer-Emmett-Teller (BET) method.

Fabrication and Electrochemical study on all the electrodes in a conventional three-electrode system: All electrochemical performances were carried out on Arbin-BT2000 electrochemical instrument in a conventional three-electrode system equipped with platinum electrode, a Hg/HgO as counter and reference electrode, respectively. Before electrochemical measurement, we have purged out O_2 from the solution by the inert gas-Ar. The working electrode was made from mixing of active materials, acetylene black, and PTFE (polytetrafluoroethylene) with a weight ratio of 75:15:10, coating on a piece of foamed nickel foam of about 1 cm^2, and being pressed it to a thin foil at a pressure of 5.0 MPa. The typical mass load of the electrode material was 5.0 mg. The electrolyte was 3.0 M KOH solutions. Galvanostatic charge–discharge methods were used to investigate capacitive properties of all the electrodes, which were all carried out with an Arbin-BT2000 electrochemical instrument. Cyclic voltammetry measurements of all the electrodes were conducted by using PARSTAT2273.

Fabrication and Electrochemical study of the flexible solid-state ASCs: The PET substrates were firstly deposited with a layer of Pt film (~3×5 nm thick) and then coated with the slurry containing the active materials [The microporous $Ni_{11}(HPO_3)_8(OH)_6$ nanocrystals or graphene nanosheets via a similar process to that in the three electrode system and were used as the working electrode after drying. The mass ratio between positive electrode and negative electrode active materials is 1:3. At the meantime, the PVA/KOH gel electrolyte was prepared as follows: the gel electrolyte (1.52 g PVA, 2.13 g KOH, and 15 mL DI water) was prepared at 75 °C for 30 min and dropped onto the prepared sample to cover the active material after it was cooled naturally. Subsequently, two pieces of such electrodes were immersed in the PVA/KOH gel solution for 5~10 min to adsorb a layer of solid electrolyte. After the excess water was vaporized, two pieces of such electrodes containing electrolyte were pressed together on a sheet out roller. Thus, the stacked all-solid-state ASCs were fabricated. CV measurements were carried out between 0 and 1.40 V on an electrochemical work station (PARSTAT2273). The flexible solid-state ASCs were galvano statically charged and discharged at the current density of 0.5-5.0 $mA \cdot cm^{-2}$ in the voltage range of 0-1.40 V on the Arbin-BT2000 electrochemical instrument. All the electrochemical measurements were conducted at room temperature.

Acknowledgements

This work is supported by the Program for New Century Excellent Talents of the University in China (grant no. **NCET**-13-0645) and National Natural Science Foundation of China (**NSFC**-21201010, U1304504), Program for Innovative Research Team (in Science and Technology) in University of Henan Province (14IRTSTHN004), the Science & Technology Foundation of Henan Province (122102210253, 13A150019, 14B150001 and 14A430038), and the China Postdoctoral Science Foundation (2012M521115) and the opening research foundations of the State Key Laboratory of Coordination Chemistry (Nanjing University).

Notes and references

[a] College of Chemistry and Chemical Engineering, Anyang Normal University, Anyang, 455002, Henan, P. R. China.
[b] State Key Laboratory of Coordination Chemistry, Nanjing University, Nanjing, 210093, Jiangsu, P. R. China.
[*] E-mail: huanpangchem@hotmail.com
Homepage: http://huanpangchem.wix.com/advanced-material

Electronic Supplementary Information (ESI) available: [details of any supplementary information available should be included here]. See DOI: 10.1039/c000000x/

1 C. Chen, W. Chen, J. Lu, D. Chu, Z. Huo, Q. Peng and Y. Li, *Angew. Chem., Int. Ed.*, 2009, **48**, 4816.
2 C. Morgovan, E. Marian, A. Iovi, I. Bratu and G. Borodi, *Rev. Chim.*, 2009, **60**, 1282.
3 H. Jiang, T. Zhao, C. Li and J. Ma, *J. Mater. Chem.*, 2011, **21**, 3818.
4 I. S. Cho, D. W. Kim, S. Lee, C. H. Kwak, S. T. Bae, J. H. Noh, S. H. Yoon, H. S. Jung, D. W. Kim and K. S. Hong, *Adv. Funct. Mater.*, 2008, **18**, 2154.
5 Z. J. Gu, T. Y. Zhai, B. F. Gao, G. J. Zhang, D. M. Ke, Y. Ma and J. N. Yao, *Crystal Growth & Design*, 2007, **7**, 827.
6 M. D. Marcos, P. Amoros and A. Ball, *J. Solid State Chem.*, 1993, **107**, 250.
7 M. D. Marcos, P. Amoros, A. Porter, R. Manez and J. P. Attfield, *Chem. Mater.*, 1993, **5**, 121.
8 S. G. Carling, P. Day and D. Visser, *Inorg. Chem.*, 1995, **34**, 3917.
9 A. Q. Yuan, J. Wu, L. J. Bai, S. M. Ma, Z. Y. Huang and Z. F. Tong, *J. Chem. Eng. Data.*, 2008, **53**, 1066.
10 C. F. Zeng, W. W. Ji and L. X. Zhang, *CrystEngComm*, 2012, **14**, 3008.
11 Y. M. Leeuwen, K. P. Velikov and W. K. Kegel, *RSC Adv.*, 2012, **2**, 2534.
12 S. Okada, S. Sawa, M. Egashira, J. Yamaki, M. Tabuchi, H. Kageyama, T. Konishi and A. Yoshino, *J. Power Sources*, 2001, **97-98**, 430.
13 A. Yamada, M. Hosoya, S. C. Chung, Y. Kudo, K. Hinokuma, K. Y. Liu and Y. Nishi, *J. Power Sources*, 2003, **119-121**, 232.
14 C. Y. Nan, J. Lu, C. Chen, Q. Peng and Y. D. Li, *J. Mater. Chem.*, 2011, **21**, 9994.
15 X. Wang, J. Zhuang, Q. Peng and Y. D. Li, *Nature*, 2005, **437**, 121.
16 J. Yu, A. J. Wang, J. Tan, X. Li, J. A. Bokhovenb and Y. K. Hua, *J. Mater. Chem.*, 2008, **18**, 3601.
17 Y. Zhao, Y. P. Zhao, H. S. Feng and J. Y. Shen, *J. Mater. Chem.*, 2011, **21**, 8137.
18 H. Wu, Y. Gao and H. M. Li, *CrystEngComm*, 2010, **12**, 3607.
19 H. Pang, Z. Z. Yan, Y. Wei, X. Li, J. Li, L. Zhang, J. Chen, J. S. Zhang and H. H. Zheng, *Part. Part. Syst. Charact.*, 2013, **30**, 287-295.
20 H. Pang, Y. Liu, Y. Ma, G. Li, Y. Ai, J. Chen, J. Zhang, H. H. Zheng, *Nanoscale*, 2013, **5**, 503-507
21 H. Pang, C. Wei, Y. Ma, S. Zhao, G. Li, J. Zhang, J. Chen and S. J. Li, *ChemPlusChem*, 2013, **78**, 546
22 S. Bai, C. Sun, P. B. Wan, C. Wang, R. Luo, Y. Li, J. F. Liu and X. M. Sun, *Small*, 2014, 10.1002/smll.201401865.

23 Q. Du, M. B. Zheng, L. Zhang, Y. Wang, J. Chen, L. Xue, W. Dai, G. Ji and J. M. Cao, *Electrochimica Acta*, 2010, **55**, 3897.
24 Z. B. Lei, J. T. Zhang and X. S. Zhao, *J. Mater. Chem.*, 2012, **22**, 153.
25 Z. Y. Lu, Z. Chang, W. Zhu and X. M. Sun, *Chem. Commun.*, 2011, **47**, 9651.
26 Z. S. Wu, W. C. Ren, D. W. Wang, F. Li, B. L. Liu and H. M. Cheng, *ACS Nano*, 2010, **4**, 5835.
27 J. Yan, Z. J. Fan, W. Sun, G. Q. Ning, T. Wei, Q. Zhang, R. F. Zhang, L. J. Zhi and F. Wei, *Adv. Funct. Mater.*, 2012, **22**, 2632.
28 Y. G. Wang, D. Zhou, D. Zhao, M. Hou, C. Wang and Y. Y. Xia, *J. Electrochem. Soc.*, 2013, **160**, A98.
29 X. L. Dong, Z. Y. Guo, Y. F. Song, M. Y. Hou, J. Q. Wang, Y. G. Wang and Y. Y. Xia, *Adv. Funct. Mater.*, 2014, **24**, 3405.
30 X. H. Lu, M. H. Yu, G. M. Wang, T. Zhai, S. L. Xie, Y. C. Ling, Y. X. Tong and Yat Li, *Adv. Mater.*, 2013, **25**, 267-272.
31 C. Zhang, H. Yin, M. Han, Z. Dai, H. Pang, Y. Zheng, Y. Q. Lan and J. Bao, J. Zhu, *ACS Nano*, 2014, **8**, 3761-3770.
32 M. F. El-Kady, V. Strong, S. Dubin and R. B. Kaner, *Science*, 2012, **335**, 1326-1330.
33 X. H. Lu, M. Yu, T. Zhai, G. Wang, S. Xie, T. Liu, C. Liang, Y. Tong and Y. Li, *Nano Lett.*, 2013, **13**, 2628-2633.
34 P. Yang, X. Xiao, Y. Li, Y. Ding, P. Qiang, X. Tan, W. Mai, Z. Lin, W. Wu, T. Li, H. Jin, P. Liu, J. Zhou, C. P. Wong and Z. L. Wang, *ACS Nano*, 2013, 7, 2617-2626.
35 X. Xiao, X. Peng, H. Jin, T. Li, C. Zhang, B. Gao, B. Hu, K. Huo and J. Zhou, *Adv. Mater.*, 2013, **25**, 5091-5097.
36 W. Zilong, Z. Zhu, J. Qiu and S. Yang, *J. Mater. Chem. C*, 2014, **2**, 1331-1336.
37 X. H. Lu, Y. X. Zeng, M. H. Yu, T. Zhai, C. L. Liang, S. L. Xie, M.-S. Balogun and Y. X. Tong, *Adv. Mater.*, 2014, **26**, 3148-3155.
38 B. G. Choi, S. J. Chang, H. W. Kang, C. P. Park, H. J. Kim, W. H. Hong, S. G. Lee and Y. S. Huh, *Nanoscale*, 2012, 4, 4983-4988.
39 J. Ren, L. Li, C. Chen, X. Chen, Z. Cai, L. Qiu, Y. Wang, X. Zhu and H. Peng, *Adv. Mater.*, 2013, 25, 1155-1159.
40 C. Z. Meng, C. H. Liu, L. Z. Chen, C. H. Hu and S. S. Fan, *Nano Lett.*, 2010, **10**, 4025-4031.

ToC

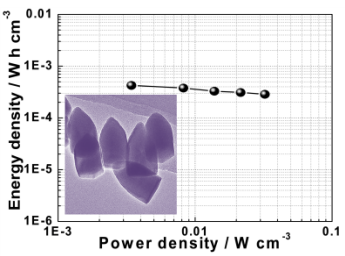

Microporous $Ni_{11}(HPO_3)_8(OH)_6$ nanocrystals are successfully applied for a flexible solid-state asymmetric supercapacitor, which can achieve a maximum energy density of 0.45 mWh·cm^{-3} with high cycle stability for 10000 cycles.